

Research Article

Improved Continuous Wavelet Transform for Modal Parameter Identification of Long-Span Bridges

Mingjin Zhang,¹ Xu Huang,¹ Yongle Li ,¹ Hao Sun,² Jingyu Zhang ,¹ and Bin Huang³

¹Department of Bridge Engineering, Southwest Jiaotong University, Chengdu 610031, Sichuan, China

²CCCC Second Highway Consultants Co., Ltd., Wuhan 430056, Hubei, China

³Sichuan Yakang Expressway Co., Ltd., 610041 Chengdu, Sichuan, China

Correspondence should be addressed to Jingyu Zhang; zhangjydc@live.com

Received 3 August 2019; Revised 27 December 2019; Accepted 2 January 2020; Published 27 January 2020

Academic Editor: Hamid Toopchi-Nezhad

Copyright © 2020 Mingjin Zhang et al. This is an open access article distributed under the Creative Commons Attribution License, which permits unrestricted use, distribution, and reproduction in any medium, provided the original work is properly cited.

Accurate and timely identification of modal parameters of long-span bridges is important for bridge health monitoring and wind tunnel tests. Wavelet analysis is one of the most advantageous methods for identification because of its good localization characteristics in both time and frequency domain. In recent years, the wavelet method has been applied more frequently in parameter identification of linear and nonlinear systems. In this article, based on wavelet ridges and wavelet skeleton, the improved modal parameter identification method was studied. To find the appropriate time-frequency resolution, an optimal wavelet basis design principle based on minimum Shannon entropy was proposed. Aiming at endpoint effect in wavelet transform, a prediction continuation method based on support vector machine (SVM) was proposed, which can effectively suppress the endpoint effect of the extended samples. In view of the fact that the ridges of metric matrices obtained by the traditional crazy climber algorithm cannot fully reflect the distribution of ridges of modulus value matrices of wavelet coefficients, an improved high-precision crazy climber algorithm was put forward to accurately identify the position of the ridge of wavelet coefficients. Finally, taking a long-span cable-stayed bridge and a long-span suspension bridge as the engineering background, improved continuous wavelet transform (CWT) was applied to modal parameter identification of bridge under ambient excitation. The modal parameters such as modal frequency, damping ratio, and mode shape were obtained. Compared with the calculation value of the numerical simulation of long-span cable-stayed bridge and wind tunnel test of long-span suspension bridge, the reliability of CWT for modal parameter identification of long-span bridges under ambient excitation was verified.

1. Introduction

In the last few decades, for the innovative tools for understanding and the optimization of design and assessment of structural health, the modal parameter identification is becoming more and more important [1]. The structural modal parameters, which could affect the design of structures, include natural frequencies, damping ratios, and mode shape vectors [2, 3]. The development of related technology has a very positive significance for the bridge structure in the complex environment [4]. The accurate identification of modes is beneficial to the dynamic response analysis of bridges in various environments [5–7]. There were various

techniques used for signal decomposition in determining the bridge modal parameter identification, such as empirical mode decomposition (EMD), stochastic subspace identification (SSI), and wavelet transform (WT). Based on field measurement data, the dynamic response and the model parameters of a cable-stayed bridge were carried out [8, 9].

Because of the ability of decomposing the nonlinear and nonstationary signal, empirical mode decomposition was an adaptive signal decomposition method [10, 11]. However, some aspects need to be improved in the original EMD like the recurrent emergence of mode mixing because of the signal intermittence, and a single intrinsic mode function (IMF) either consists of signals of widely disparate scales or

signals of similar scale residing in a different IMF [11]. Huang et al. [10] introduced the intermittence test. To overwhelm the scale separation problem, a new method based on the statistical studies of white noise called ensemble EMD (EEMD) was introduced by Wu and Huang [11]. The EEMD defines the IMF component as a mean of an ensemble of trails having signal as well as white noise of finite amplitude [11]. The new concept of white noise was also investigated ([12–14]). Yeh et al. [15] introduced the complimentary EEMD to improve the computation efficiency.

During the past few years, the stochastic subspace identification (SSI) has been successfully applied on the structures for output-only system identification. There are basically two important numerical tools for subspace methods in linear algebra, one is the singular value decomposition (SVD) and the other is the QR decomposition [16]. For large-scale civil structures such as long-span bridges, the output-only SSI is very effective for identification and monitoring of these vibrations of structures because of ambient. Therefore, there are various SSI techniques such as covariance-driven SSI, data-driven SSI (DATA-SSI), and combination of others methods, like expectation maximization technique (EM-SSI) [17, 18]. DATA-SSI algorithms were fully enhanced [19]. The main output-only identification in the DATA-SSI techniques is the orthogonal projections performed by LQ decomposition [19, 20]. Then, it is followed by the SVD to extract the subspace system. In DATA-SSI, there are variants which correspond to different choices for weighting the matrices before factorization of the projection matrix. Then, Weng et al. [21] studied the DATA-SSI to investigate the dynamic characteristics.

Since the introduction of wavelet theory was put forward in the 1980s [22], the application of wavelet transform has penetrated in various fields. Gurley and Kareem [23] systematically summarized the application of wavelet transform in civil engineering. The WT method can achieve automatic decoupling of low-frequency dense modal of multi-degree-of-freedom systems with its good time-frequency resolution. Many scholars have also done a lot of research on identifying structural modal parameters by using the WT method [24–27]. Based on a long-span cable-stayed bridge, which was excited by typhoon Haikui, the model parameters including frequency and damping ratio were identified using the WT method [28].

To find a suitable time-frequency resolution, this article proposed an optimal wavelet basis design method based on minimum Shannon entropy. The method of structural modal parameter identification based on wavelet ridges and wavelet skeleton was discussed in detail. A method called “predictive continuation” based on support vector machine (SVM) was proposed to control the endpoint effect in wavelet transform, and the suppress effect is verified by comparing the R^2 of the logarithmic curve of wavelet ridge amplitude and the least square curve before and after the extension. Because the metric matrix wavelet ridges obtained by the traditional crazy climber algorithm cannot fully reflect the

distribution of the wavelet coefficient modulus matrix wavelet ridges, to accurately identify the position of wavelet ridge, the traditional crazy clipper algorithm was improved. Finally, a long-span cable-stayed bridge with numerical simulation and a long-span suspension bridge for wind tunnel test were taken as the engineering background to verify the improved continuous wavelet transform method for modal parameter identification.

2. Identification of Modal Parameters by Continuous Wavelet Transform

For an arbitrary time series $f(t) \in L^2(R)$, the continuous wavelet transformation coefficient $W(a, b)$ is defined as follows:

$$\begin{aligned} W_\psi(a, b) &= \langle f(t), \psi_{a,b}(t) \rangle = \int_{-\infty}^{+\infty} f(t) \cdot \psi_{a,b}^*(t) dt \\ &= \frac{1}{\sqrt{a}} \int_{-\infty}^{+\infty} f(t) \cdot \psi_{a,b}^*\left(\frac{t-b}{a}\right) dt, \end{aligned} \quad (1)$$

where $\psi_{a,b}^*$ means the conjugate $\psi_{a,b}$.

For the multi-degree-of-freedom viscous damped system shown in Figure 1, the free response signal is as follows:

$$x(t) = \sum_{i=1}^k A_i e^{-\xi_i \omega_i t} \cos(\omega_{di} t + \phi_i), \quad (2)$$

where ω_i and ω_{di} are the i th order natural frequencies of the system without damping and with damping, respectively, and ξ_i is the damping ratio. The relationship among them is as follows:

$$\omega_{di} = \omega_i \sqrt{1 - \xi_i^2}. \quad (3)$$

Continuous wavelet transformation for $x(t)$ is also carried out, and the wavelet coefficient is as follows:

$$W_\psi(a, b) = \frac{\sqrt{a}}{2} \sum_{i=1}^k A_i e^{-\xi_i \omega_i b} \hat{\psi}^*(a \omega_{di}) e^{j(\omega_{di} b + \phi_i)}. \quad (4)$$

Wavelet coefficients reflect the similarity between wavelet basis and signal to be recognized. Therefore, from equation (4), for a fixed scale factor a_i , the $W_\psi(a, b)$ gets the maximum value only when $a_i \omega_{di} = \omega_c$.

$$|W_\psi(a_i, b)| = \frac{\sqrt{a_i}}{2} A_i e^{-\xi_i \omega_i b} |\hat{\psi}^*(a_i \omega_{di})|. \quad (5)$$

Taking the logarithm operation for equation (5), and then doing derivation for the translation factor b :

$$\begin{aligned} \ln|W_\psi(a_i, b)| &= -\xi_i \omega_i b + \ln\left(\frac{\sqrt{a_i}}{2} A_i |\hat{\psi}^*(a_i \omega_{di})|\right), \\ k_1 &= \frac{d(\ln|W_\psi(a_i, b)|)}{db} = -\xi_i \omega_i. \end{aligned} \quad (6)$$

Similarly, equation (7) shows the deviation of the phase of wavelet coefficients:

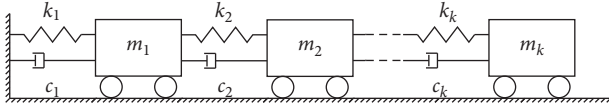


FIGURE 1: Viscous damping system of multiple degrees of freedom.

$$\begin{aligned} \angle |W_\psi(a_i, b)| &= \omega_{di} b + \phi_i, \\ k_2 &= \frac{d|W_\psi(a_i, b)|}{db} = \omega_{di}. \end{aligned} \quad (7)$$

Simultaneous equations (3), (6), and (7); the system's i th order undamped frequency f_i ; and the damping ratio ξ_i can be obtained as follows:

$$\begin{aligned} f_i &= \frac{\sqrt{k_1^2 + k_2^2}}{2\pi}, \\ \xi_i &= \frac{-k_1}{2\pi f_i}. \end{aligned} \quad (8)$$

3. Improved Continuous Wavelet Transform Algorithm

3.1. Optimal Wavelet Basis Design Based on Minimum Shannon Entropy. The complex Morlet wavelet contains time window and frequency window which corresponds to temporal resolution and frequency resolution, respectively. For two adjacent frequencies f_i and f_{i+1} , the frequency interval is $\Delta f_i = f_{i+1} - f_i$ and the average value is \bar{f}_i . The relationship between the wavelet's scale factor a at \bar{f}_i and the mother wavelet center frequency f_c can be written as

$$a = \frac{f_c}{\bar{f}_i}. \quad (9)$$

Frequency resolution df is

$$df = 2\Delta f = \frac{1}{\pi a \sqrt{f_b}} = \frac{\bar{f}_i}{f_c} \cdot \frac{1}{\pi \sqrt{f_b}}. \quad (10)$$

Therefore, to decouple the adjacent two-order modals, the following conditions must be satisfied.

$$\begin{aligned} \Delta f_i &\geq \alpha \cdot df = \alpha \cdot \frac{\bar{f}_i}{f_c} \cdot \frac{1}{\pi \sqrt{f_b}}, \\ f_c \sqrt{f_b} &\geq \alpha \cdot \frac{\bar{f}_i}{\pi \Delta f_i}, \end{aligned} \quad (11)$$

where α is a custom parameter; generally, the adjacent modal frequencies can be decoupled when $\alpha = 2$ [29]. It can be seen from equation (11) that multiple f_b meet the dense modal decoupling requirements when the mother wavelet center frequency f_c is determined and the dense modal decoupling ability is stronger when f_b is larger. However, because of the time-frequency window area of wavelet being fixed, excessive frequency resolution can cause a very small time resolution, which leads to obvious

endpoint effect. To eliminate this effect, this article introduced the concept of Shannon value. Shannon reflects the degree of the order of the probability distribution sequence, and the smaller the Shannon value the more orderly the distribution and the stronger the regularity of information. Therefore, when Shannon value of the wavelet coefficient reaches the minimum, the corresponding wavelet basis is most similar to the characteristic component of the analysis signal, where f_c and f_b are the optimal parameters.

Suppose $WT(a_i, t)$ as a series of wavelet coefficients obtained when the scale factors are a_1, a_2, \dots, a_n . The energy of the wavelet coefficient at each scale is

$$E_i = \sum_t |WT(a_i, t)|^2. \quad (12)$$

The Shannon value of the wavelet coefficient is

$$E = - \sum_i^n p_i \log p_i, \quad (13)$$

where

$$p_i = \frac{E_i}{\sum_{i=1}^n E_i}, \quad (14)$$

where p_i indicates the probability distribution of the energy of the wavelet coefficients at the a_i scale and the set is the probability distribution sequence of the energy of the wavelet coefficient at each scale.

In this article, MATLAB method is used to simulate the free decay response signal of a two-degree-of-freedom viscous damping system. The sampling frequency is 100 Hz, and the sampling time is 10 s. The theoretical frequency and damping ratio of the system are given in Table 1. The time domain and the frequency curve of the signal are shown in Figure 2.

In this system, according to equation (11), it is necessary to satisfy $f_c \sqrt{f_b} \geq 1.49$ to decouple the two-order modal. When $f_c = 5$ Hz, $f_b \in [1, 50]$, the relationship between the Shannon value of the wavelet coefficient and f_b is shown in Figure 3. It can be seen that when $f_b = 42$, the Shannon value of wavelet coefficient for the system is the smallest, and the time-frequency distribution of the corresponding wavelet coefficient modal is shown in Figure 4(c). In addition, the time-frequency distributions of wavelet coefficients when $f_b = 0.1$ and $f_b = 1$ are shown as Figures 4(a) and 4(b), respectively.

From Figure 4, the wavelet transform is not enough to decouple the two-order modal frequencies when $f_b = 0.1$ and two obvious wavelet ridges cannot be found in Figure 4(a), while f_b is equal to 1 and 42, the wavelet transform can decouple the two-order modal. However, from Figure 4(c) two elongated wavelet ridges can be clearly seen, and there are only two fuzzy wavelet ridges in Figure 4(b). It can be proved that the decoupling effect when $f_b = 42$ is better than that when $f_b = 1$. Therefore, optimal wavelet basis design based on the minimum Shannon can easily find a suitable bandwidth parameter f_b , and construct a wavelet basis for wavelet transform to achieve dense modal

TABLE 1: Simulation system theoretical frequency and damping ratio.

Order	Frequency (Hz)	Damping ratio
1	0.44	0.02
2	0.68	0.02

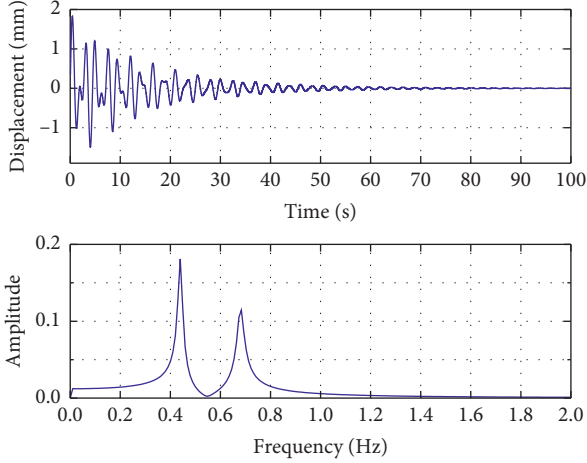


FIGURE 2: Free decay response signal of simulation system: time domain (a) and frequency domain (b).

decoupling of the analysis signal, and a better solution coupling effect can be guaranteed.

3.2. Endpoint Effect Suppression Based on SVM Prediction Extension. For large civil engineering structures such as long-span bridges, the natural frequency is generally low. The wavelet transforms with larger time window will produce obvious endpoint effect. At present, the intermediate unaffected wavelet coefficients after wavelet transform for modal identification are used to eliminate the endpoint effect. However, for short samples with limited data, there are not much data left after the interception, which causes inefficient use of data and decreases the recognition accuracy. To avoid this situation, regression prediction method based on support vector machine (SVM) was used to extend the data. The extended data obtained by this method not only retain the characteristics of the original signal but also ensure its continuity and derivative.

The natural excitation method was used to obtain the vertical response at midspan of bridge. The sample time was set to 30 s, and the sampling frequency of the impulse response was 100 Hz. All impulse response data were divided into 200 samples and trained each sample with SVM method, and 1000 data points were predicted and extended at both ends, respectively. The obtained extended curve is shown in Figure 5; the blue line means the original data and the red line means the predicted extension data.

The optimal wavelet basis was used to perform the continuous wavelet transform on the unexpanded impulse response data and the extended data, and the corresponding wavelet coefficient was obtained. For the wavelet coefficient

of the extended data, the amplitude logarithmic curves of the first three-order wavelet ridges after removing the extension part are presented in Figure 6. The solid blue line represents the amplitude logarithmic curve of the wavelet coefficient, whereas the red dashed line means its least square linear fitted curve. From equations (6) to (8), it can be known that the accuracy of the curve fitted is directly related to the accuracy of the identified modal parameters. The R^2 of wavelet ridge amplitude logarithmic curve and least square curve is shown in Table 2. Comparing the amplitude logarithmic curves before and after the extension, the endpoint effect of each order of modal is well suppressed and the quality of fitted curve is also improved. Table 2 shows that R^2 of first order increased from 0.6513 to 0.9214, R^2 of second order increased from 0.8003 to 0.9392, and R^2 of third order increased from 0.8728 to 0.9951. For the first-order modal, the suppress effect of the endpoint effect is increased by 41.5%. For the high-order modal, because the wavelet time window is small, the data expansion can basically eliminate the endpoint effect. Therefore, using SVM to expand the sample data can effectively reduce the endpoint effect.

3.3. Extracting Wavelet Ridges Based on Improved Crazy Climber Algorithm

3.3.1. Traditional Crazy Climber Algorithm. It is assumed that the wavelet coefficient modulus matrix obtained by wavelet transform is $M \in R^{V \times H}$, where V means the number of rows for the matrix, indicating the vertical direction [10, 11], and H means the number of columns for the matrix, indicating the horizontal direction. Referring to the definition of Cartesian coordinate system, $M(i, j)$ is defined as the j th row and i th column element in the matrix, where $i \in [1, 2, \dots, H]$, $j \in [1, 2, \dots, V]$. In addition, a metric matrix D of the same size as the M matrix is defined. When each climber in the modulus matrix is moved once, the corresponding modulo value is superimposed at the corresponding position of the metric matrix D . Before calculation, the metric matrix is initialized to 0 and N climbers are generated; all climbers are randomly distributed in the M matrix, and then climber is moved in the following steps.

Step 1: at the initial moment, set T_0 as the system initial temperature parameter, mark the initial coordinate $X_k(0)$ of each climber. And use the modulus $M(X_k(0))$ of each climber position to stack the corresponding positions of the metric matrix, where k represents the k th climber.

Step 2: at time t , the system temperature is T_t , the coordinate of climber $X_k(t) = (i, j)$, and at time $t + 1$, the coordinate $X_k(t + 1) = (i', j')$ can be determined according to the following rules.

Step 2.1: because the wavelet ridges are continuous in time, the climber in the horizontal direction moves left or right one grid with the same probability, and the coordinate is (i', j) .

Step 2.2: then, in the vertical direction, it is assumed that the climber moves up or down one grid with the

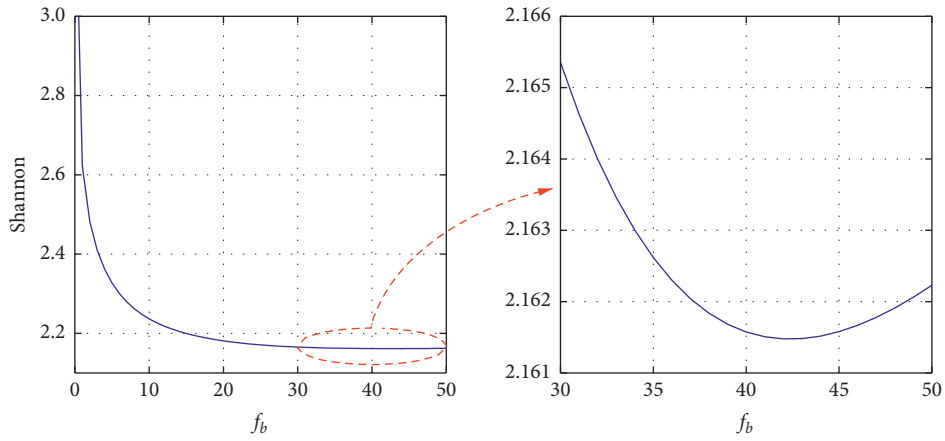


FIGURE 3: Relationship curve of Shannon and f_b .

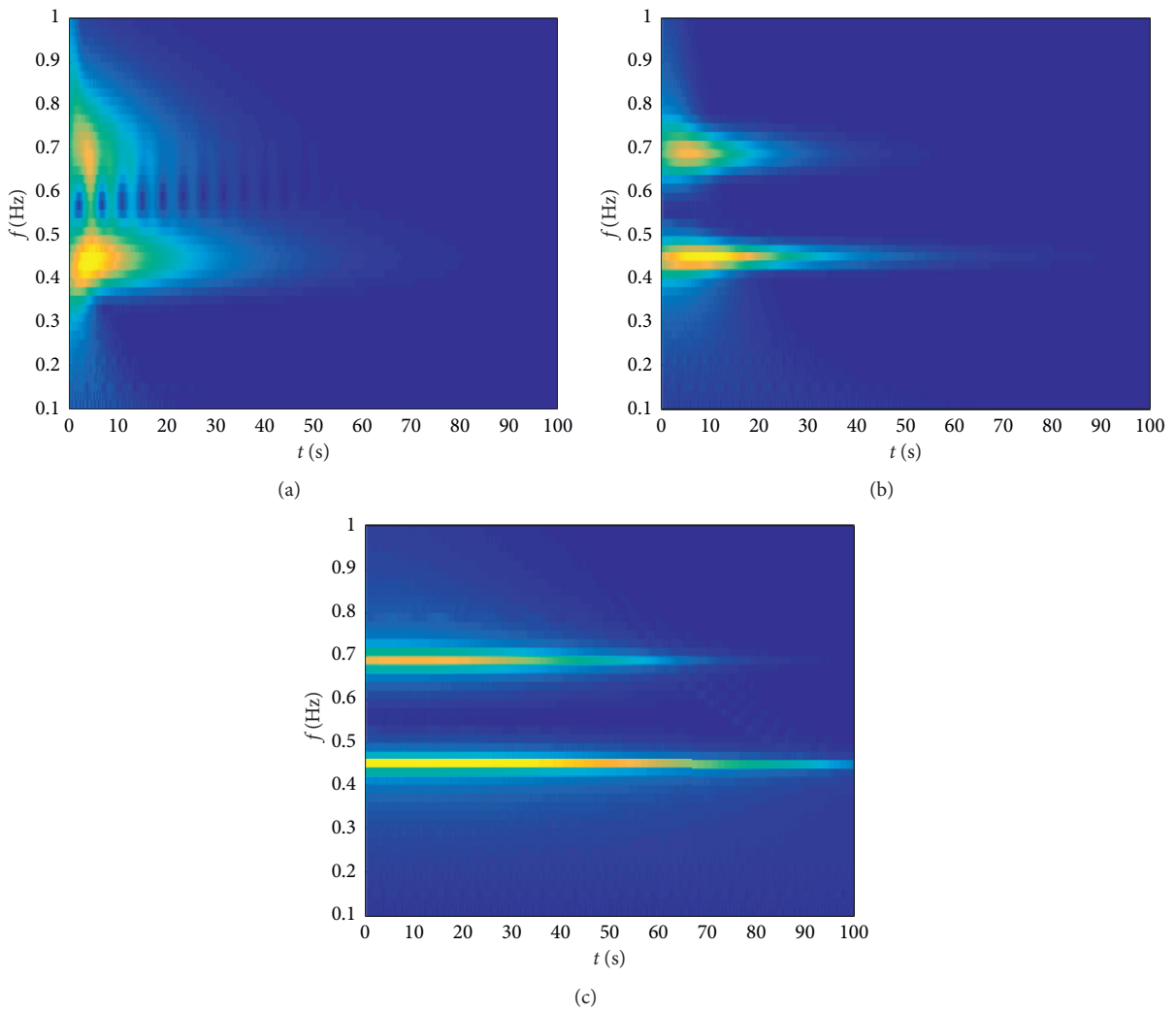


FIGURE 4: Time-frequency graph of wavelet coefficients with different f_b : (a) $f_b = 0.1$; (b) $f_b = 1$; (c) $f_b = 42$.

same probability and the coordinate after moving is (i', j') ; then follow the conditions to determine whether to move this step:

- (i) If $M(i', j') > M(i', j)$, this step should be moved in the vertical direction, and the coordinate after moving is (i', j') ;

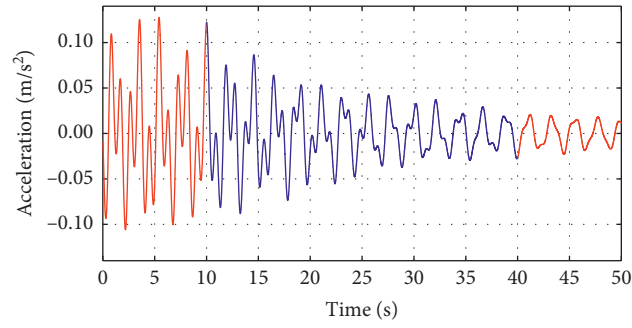


FIGURE 5: Vertical impulse response function and its extended data curve.

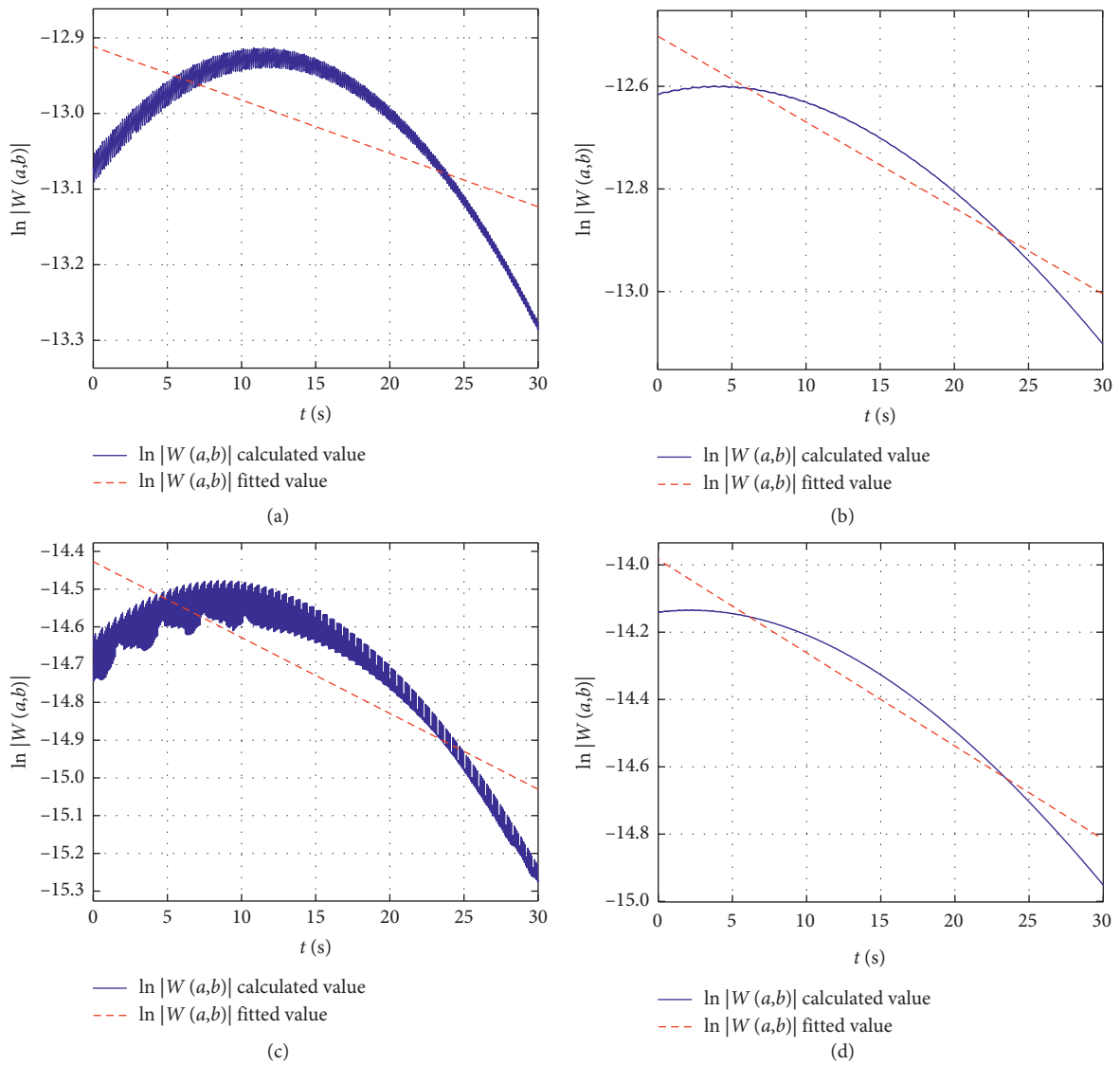


FIGURE 6: Continued.

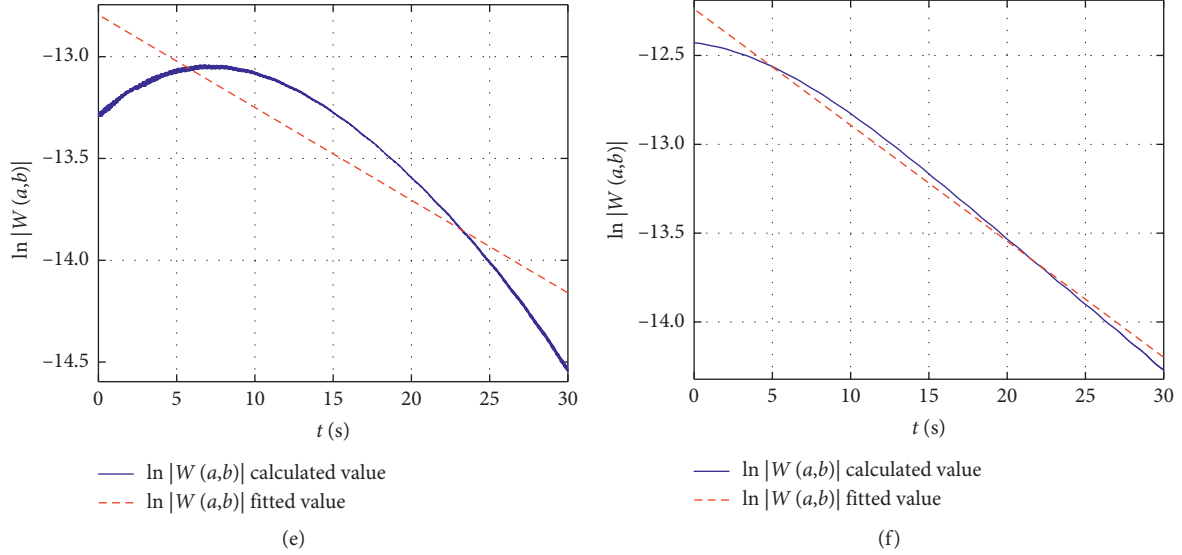


FIGURE 6: Logarithmic curve of the amplitude of wavelet coefficients up to the third orders before and after extension. (a) First order before extension. (b) First order after extension. (c) Second order before extension. (d) Second order after extension. (e) Third order before extension. (f) Third order after extension.

TABLE 2: The R -square of wavelet ridge amplitude logarithmic curve and fitted curve.

Order	R -square	
	Before extension	After extension
First	0.6513	0.9214
Second	0.8003	0.9392
Third	0.8728	0.9951

(ii) If $M(i', j') \leq M(i', j)$, there is a certain probability p to move, that is $X_k(t+1) = (i', j')$. There is also a probability of $1 - p$ that does not move, that is $X_k(t+1) = (i', j)$, where p is determined according to the following formula:

$$p = e^{[M(i', j') - M(i', j)]/T_i}. \quad (15)$$

Step 3: after the movement mentioned above ends, system temperature is updated; the corresponding positions of the metric matrix are superimposed using the modulus value $M(X_k(t+1))$ at each climber position.

Step 4: repeat steps 2 and 3 until the system temperature drops to the threshold, and terminate the iterative process to obtain the final metric matrix D .

Step 5: the ridge line can be obtained by connecting the more prominent points in the metric matrix.

3.3.2. Improved Crazy Climber Algorithm. In the traditional crazy climber algorithm, the ridge is determined by the location of the maximum value in the metric matrix D . Acquisition process of the metric matrix has certain randomness, and the distribution of modulus matrix of wavelet

coefficients cannot be fully reflected, so the extracted ridge may not be the real ridge of the system. Wavelet transform was applied on the signal shown in Figure 5, and the modulus values of the first ten columns of wavelet coefficients near the first-order ridge position are shown in Table 3. Corresponding position matrix metric obtained by the crazy climber algorithm is shown in Table 4. In the two tables, gray cells in the table represent the local maximum. Comparing the two tables, metric matrix wavelet ridges obtained by the crazy climber algorithm cannot fully reflect the distribution of the wavelet coefficient modulus matrix ridge. If only the metric matrix is used to extract the ridge of wavelets, the obtained wavelet skeleton will be quite different from the real wavelet skeleton.

Aimed at this problem, an improved crazy climber algorithm was put forward in this part. Although ridge distribution of the metric matrix does not represent the exact distribution of the wavelet ridges accurately, the distribution range basically includes the distribution range of the wavelet ridges. In addition, the crazy climber algorithm has excellent antinoise ability. Therefore, the basic idea of the improved algorithm was to use the traditional crazy climber algorithm to remove the noise interference and obtain the approximate distribution range of the wavelet ridges. Then, use the modulus maximum method to extract the exact position of the wavelet ridges within the distribution of each ridge line. The basic implementation process is as follows:

Step 1: complete steps 1 to 5 of the traditional crazy climber algorithm to obtain the ridge distribution of the metric matrix.

Step 2: determine the number n of the ridge of the measurement matrix and obtain the minimum row number $s_i = [s_1, s_2, \dots, s_n]$ and the maximum row number $e_i = [e_1, e_2, \dots, e_n]$ of each ridge.

TABLE 3: Wavelet coefficient modulus value near the first-order ridge.

Line number	Columns number							Modulus magnitude: 10^{-6}		
	1	2	3	4	5	6	7	8	9	10
20	3.083	3.085	3.091	3.093	3.095	3.097	3.099	3.100	3.101	3.102
21	3.318	3.318	3.318	3.319	3.319	3.319	3.319	3.319	3.320	3.320
22	1.142	1.142	1.142	1.141	1.141	1.141	1.141	1.141	1.141	1.141

TABLE 4: Metric matrix metric value near first-order ridge.

Line number	Columns number							Metric order of magnitude: 10^{-8}		
	1	2	3	4	5	6	7	8	9	10
20	2.920	6.037	5.658	4.980	5.863	5.475	8.217	7.633	9.104	8.029
21	3.560	5.237	6.913	5.657	6.705	6.705	6.391	9.535	6.707	7.545
22	0.685	2.054	1.730	2.450	2.090	2.306	2.666	1.910	2.883	3.387

Step 3: construct an empty matrix H_i that is consistent with the wavelet coefficient modulus value matrix M and fill the modulus values in the i th ridge distribution range $[s_i, e_i]$ in the modulus value matrix into the same position in the empty matrix H_i . Then, find out the maximum value of each column in the matrix H_i and mark the coordinates of each point.

Step 4: connect the points obtained in step 3 in the modulus value matrix to obtain the i th ridge line of the wavelet coefficients.

Step 5: repeat steps 3 and 4 until all the ridges are found.

To verify the effectiveness of the algorithm, the continuous wavelet of the optimal wavelet base is used to transform the signal shown in Figure 5, and then the wavelet coefficients are obtained. The time-frequency distribution of the wavelet coefficient after discarding the wavelet coefficient of the extension part at both ends is shown in Figure 7; the wavelet ridges obtained by the traditional crazy climber algorithm and the improved crazy climber algorithm are shown in Figure 8. Amplitude logarithmic curves of corresponding second-order wavelet coefficients are shown in Figure 9. Comparing with the two pictures in Figures 8 and 9, respectively, it can be found that the wavelet ridges and wavelet coefficient amplitude obtained by the improved crazy climber algorithm are more concentrated, which can represent the real situation of the wavelet coefficient of the analysis signal. Therefore, the improved crazy climber algorithm not only has exceptional antinoise ability but also can accurately determine the position of the wavelet ridges, so it has better practicability.

4. Verification Examples

4.1. Numerical Example

4.1.1. Dynamic Characteristic Calculation. Taking Oujiang Bridge, which is a concrete cable-stayed bridge with double pylons and double cable planes, as the engineering background, the span arrangement is 52 m + 90 m + 300 m + 90 m + 52 m, and the length of the

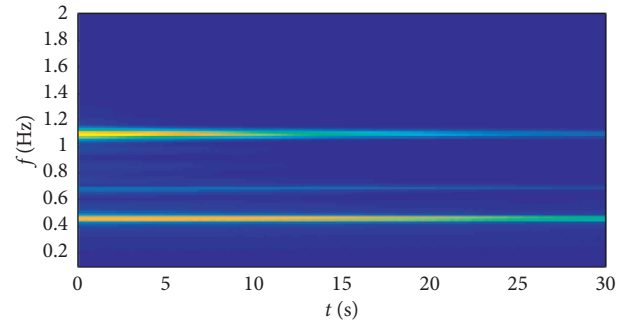


FIGURE 7: Time-frequency distribution of modulus value of wavelet coefficients.

bridge is 584 m. The width and the height of the main girder are 13 m and 4 m, respectively. The bridge adopts a space double cable plane system and fan arrangement. The diamond-shaped towers are arranged as follows: the heights of the towers are 118 m and 112.5 m, respectively, and the height above the girder is 75 m. The overall arrangement of the Oujiang Bridge is shown in Figure 10. The principal vibration frequencies and vibration modes of the bridge calculated by ANSYS are shown in Table 5.

4.1.2. Bridge Response under the Train and Fluctuating Wind Loads. The response of Oujiang Bridge under the combined action of the train and the fluctuating wind loads was calculated by using the wind-train-bridge coupling calculation and analysis software system BANSYS (bridge analysis system). The wind speed was set as 30 m/s and the train was selected as C62 freight cargos, and the speed of the train was 72 km/h. Seven measuring points along the bridge were arranged and the vertical, lateral, and torsional acceleration responses of each measuring point were also obtained. The location of the measuring points is shown in Figure 11.

The sampling frequency of each measuring point was set as 100 Hz, and the sampling time was 50 s. Figure 12 shows the acceleration response time history at the midspan measuring point (measuring point no. 4) under the combined action of fluctuating wind load and vehicle load.

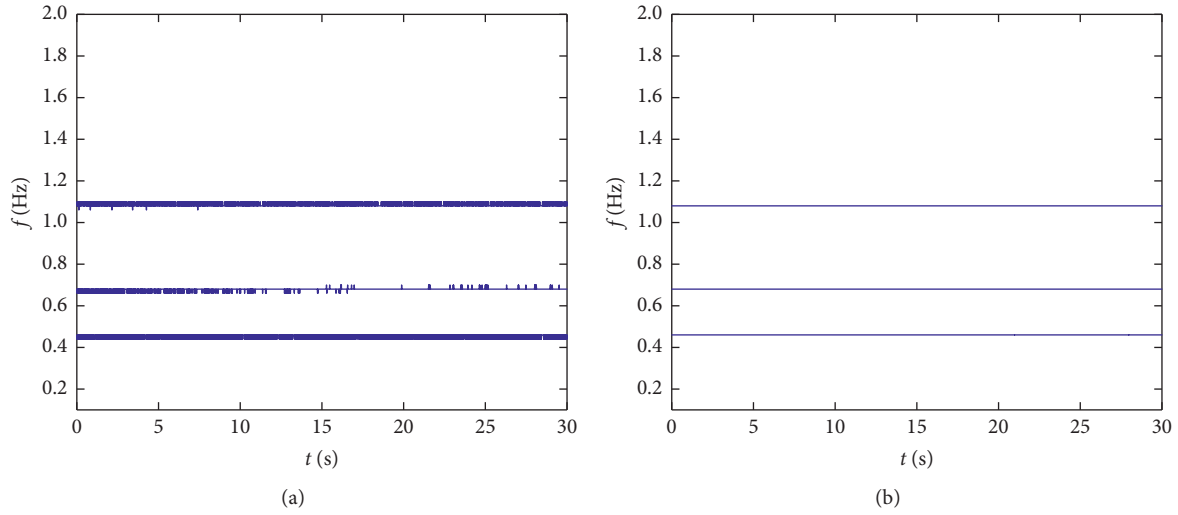


FIGURE 8: Wavelet ridges. (a) Traditional crazy climber algorithm. (b) Improved crazy climber algorithm.

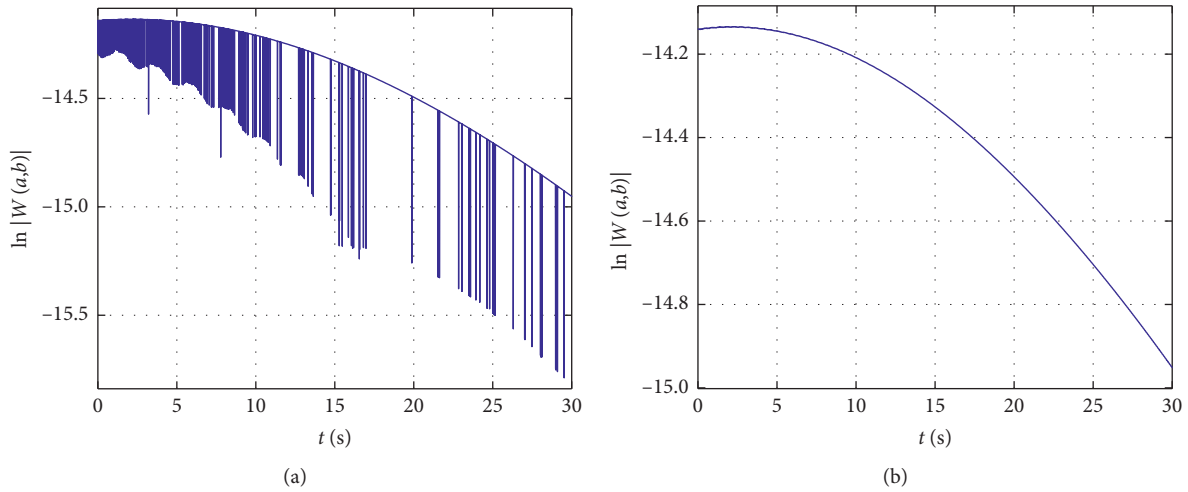


FIGURE 9: Logarithmic curve of second-order wavelet coefficient amplitude. (a) Traditional crazy climber algorithm. (b) Improved crazy climber algorithm.

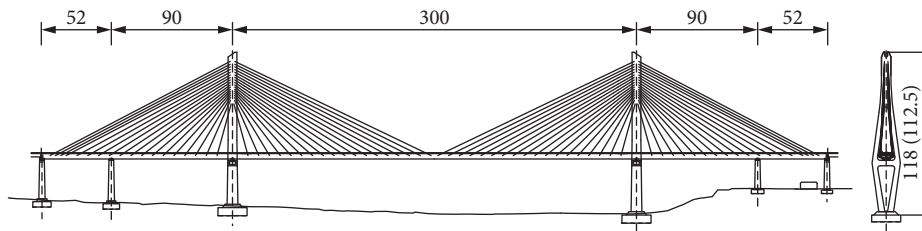


FIGURE 10: Oujiang Bridge overall layout (unit: m).

4.1.3. *Modal Parameter Identification.* The measuring point no. 4 was selected as the reference point for identification of the vertical bending modal parameter. The cross-correlation function calculated by the natural excitation method between the responses of other measuring points and the reference point is used as the free response signals of the

system. The sampling frequency was 100 Hz, and the sampling time was 30 s. Then, the SVM method was used for each free response signals, and 1000 data points were extended at both ends of the signal. The extended signal history of measuring point no. 2 and no. 4 is shown in Figure 13, respectively.

TABLE 5: Main frequency and mode of vibration.

Order	Frequency (Hz)	Mode of vibration
Vertical bend	1	Symmetrical vertical bend -1
	2	Antisymmetric vertical bend -1
	3	Symmetrical vertical bend -2
	4	Antisymmetric vertical bend -2
	5	Symmetrical vertical bend -3
	6	Symmetrical vertical bend -4
	7	Antisymmetric vertical bend -3
	8	Antisymmetric vertical bend -4
Lateral bend	1	Symmetrical lateral bend -1
	2	Antisymmetric lateral bend -1
	3	Symmetrical lateral bend -2
	4	Antisymmetric lateral bend -2
	5	Symmetrical lateral bend -3
	6	Symmetrical lateral bend -4
Torsion	1	Symmetrical torsion -1
	2	Antisymmetric torsion -1

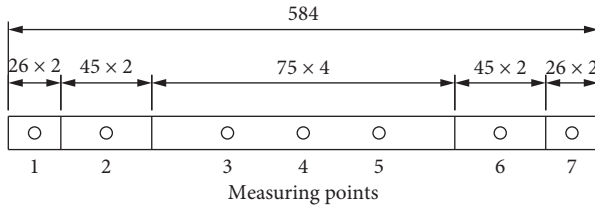


FIGURE 11: Arrangement of measuring points (unit: m).

Based on the minimum Shannon criterion of the wavelet coefficients, the parameters of the optimal complex Morlet wavelet basis function are $f_c = 4$ Hz and $f_b = 10$. Continuous wavelet transform was performed on the free response signal of each measuring point by using the optimal wavelet basis, and the wavelet coefficients of the extended part were discarded. Finally, the improved crazy climber algorithm was used to extract the wavelet ridges. The wavelet ridges of measurement point no. 2 and no. 4 are shown in Figure 14.

The wavelet coefficients of each ridge line were extracted, and the logarithmic and phase curves of the amplitude of the wavelet coefficients were plotted. The slope rate of each curve was calculated by least squares linear fitting. And, the frequencies of each order and the damping ratio of each measuring point can be calculated by equation (8). The modal parameter of the system was the average value of the modal parameters of each measuring point. For measuring point no. 2 and no. 4, the logarithmic curve, phase curve, and fitting curve of the amplitude value of each order are shown in Figure 15.

The results of vertical bend, lateral bend, and torsional modal parameters of the Oujiang Bridge are shown in Table 6. It can be seen from Table 4 that the improved continuous wavelet transform can accurately identify the

main modal parameters of long-span cable-stayed bridge, and the decoupling effect is better for low-order dense modal.

4.2. Wind Tunnel Example

4.2.1. Background Introduction. In the last section, the reliability of the proposed method is verified by numerical simulation. In this part, an aeroelastic model of full bridge was used to examine the method proposed by authors. Taking Jinshajiang Bridge of Lijiang-Shangri-La expressway as the engineering background, the main bridge of the bridge is a 766 m single span steel truss suspension bridge. The upper part of the main bridge is designed as a whole, with a stiffening girder of 26.0 m wide and 6.0 m high. The scale ratio of aeroelastic model of the bridge is 1 : 80, and the elevation design and real bridge model of aeroelastic model of the whole bridge are shown in Figure 16. The boundary conditions of the completed bridge state model of the Jinshajiang Bridge are consistent with the actual bridge, and the constraints are (1) the bottom of the bridge tower is consolidated with the rigid floor, i.e., the freedom in all six directions is constrained; (2) the main cable is connected with the rigid ground anchor, i.e., the translational freedom in all three directions is constrained; (3) the beam end of the main beam is located at the bridge tower, with the vertical displacement, the transverse displacement, and the axial displacement along the bridge Torsional degrees of freedom are constrained, and the rest are not.

4.2.2. Measurement Arrangement and Bridge Responses under Wind Load. In the aeroelastic model modal test of the whole bridge of Jinsha River bridge, the static vortex generator, distributed rough element, serrated main baffle, and additional baffle are arranged in front of the wind tunnel test section to simulate the atmospheric boundary layer and generate fluctuating wind, so as to obtain the displacement time history response signal of each measuring point of the main beam under the excitation of fluctuating wind. The measuring instrument adopts the ILD1401-200 noncontact laser displacement sensor produced by Micro-Epsilon Company, with a range of 200 mm, a static test accuracy of 40 μ m, and a sampling frequency of 1 kHz. The noncontact laser displacement sensor is shown in Figure 17, and the atmospheric boundary layer simulation device is shown in Figure 18.

To obtain the concerned modal response of each stage, 11 measuring points are arranged along the bridge span in the aeroelastic model test of Jinshajiang Bridge, and the positions of each measuring point are shown in Figure 19. During the test, the response of the bridge under the action of the fluctuating wind is collected by the laser displacement device. The sampling frequency is 128 Hz, and the duration is 128 s. Under the action of fluctuating wind, the vertical, horizontal, and torsional response time history curve of measuring point 6 is shown in Figure 20.

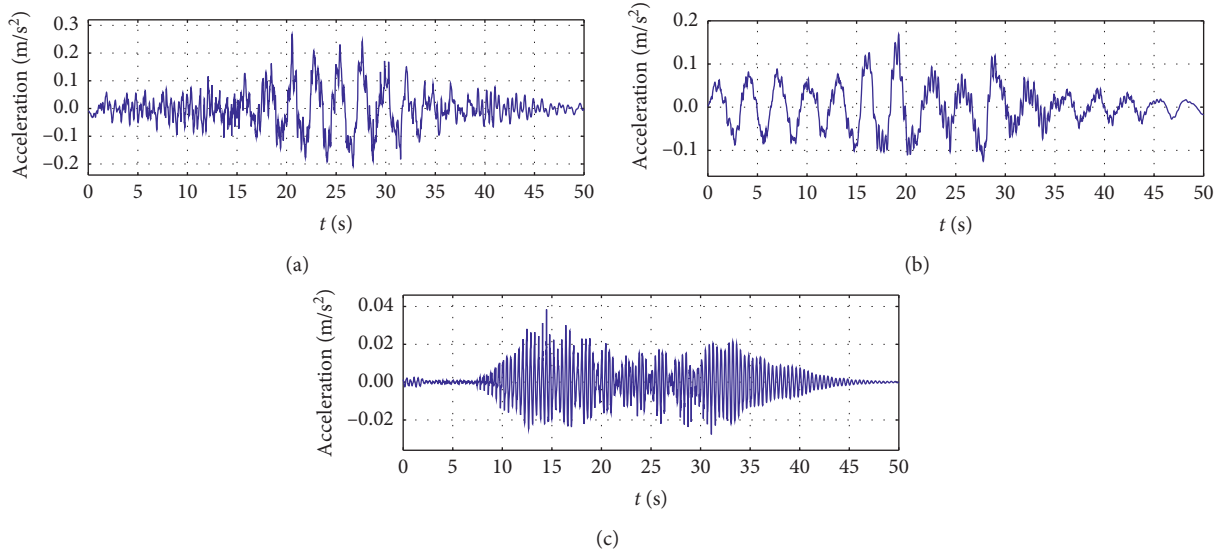


FIGURE 12: Acceleration-time curve of measuring point no. 4 (unit: m/s^2). (a) Case 1: vertical acceleration. (b) Case 1: lateral acceleration. (c) Case 1: torsion acceleration.

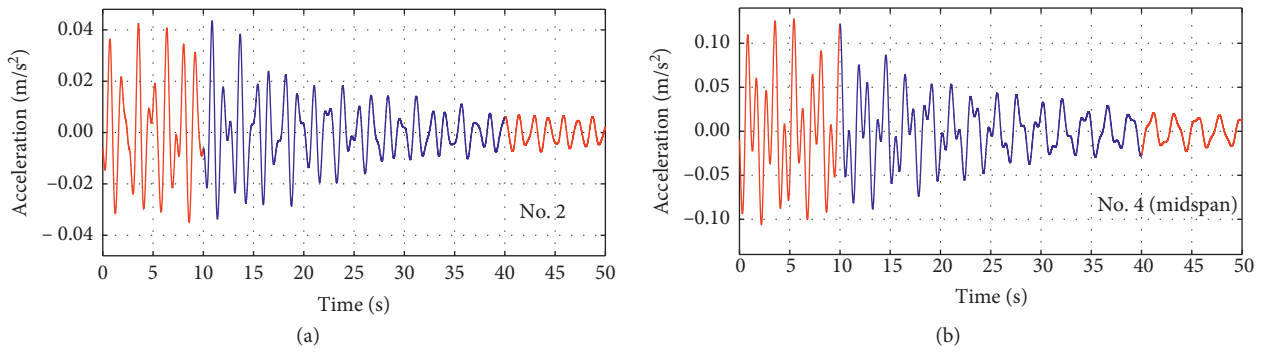


FIGURE 13: Free response signal of point no. 2 and point no. 4 with predictive extension.

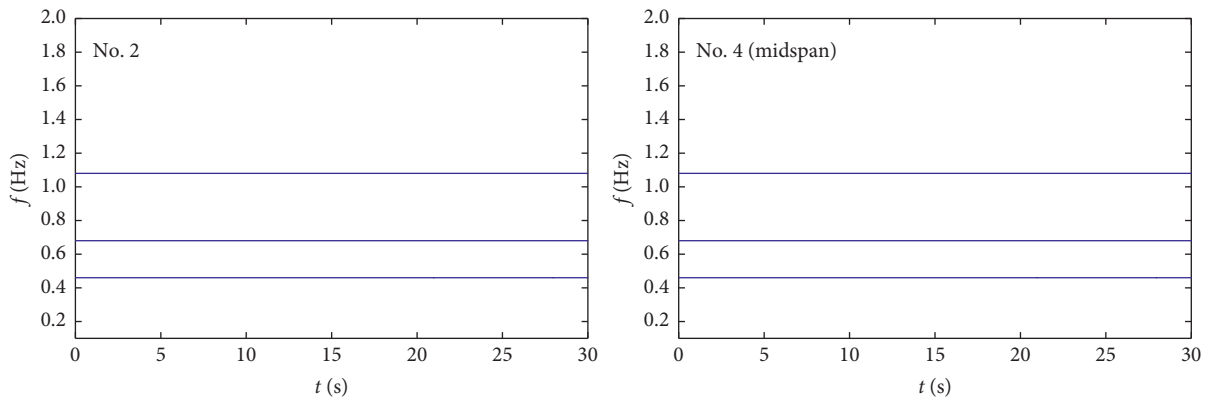


FIGURE 14: Wavelet ridges of point no. 2 and no. 4.

4.2.3. *Modal Parameter Identification.* Using the improved continuous wavelet transform for modal parameter identification, the modal parameters of the aeroelastic model of Jinshajiang Bridge are obtained as shown in Table 7. From

Table 7, it can be seen that the improved CWT can accurately identify the modal parameters of long-span suspension bridges, and has a good decoupling effect for low-order dense modes.

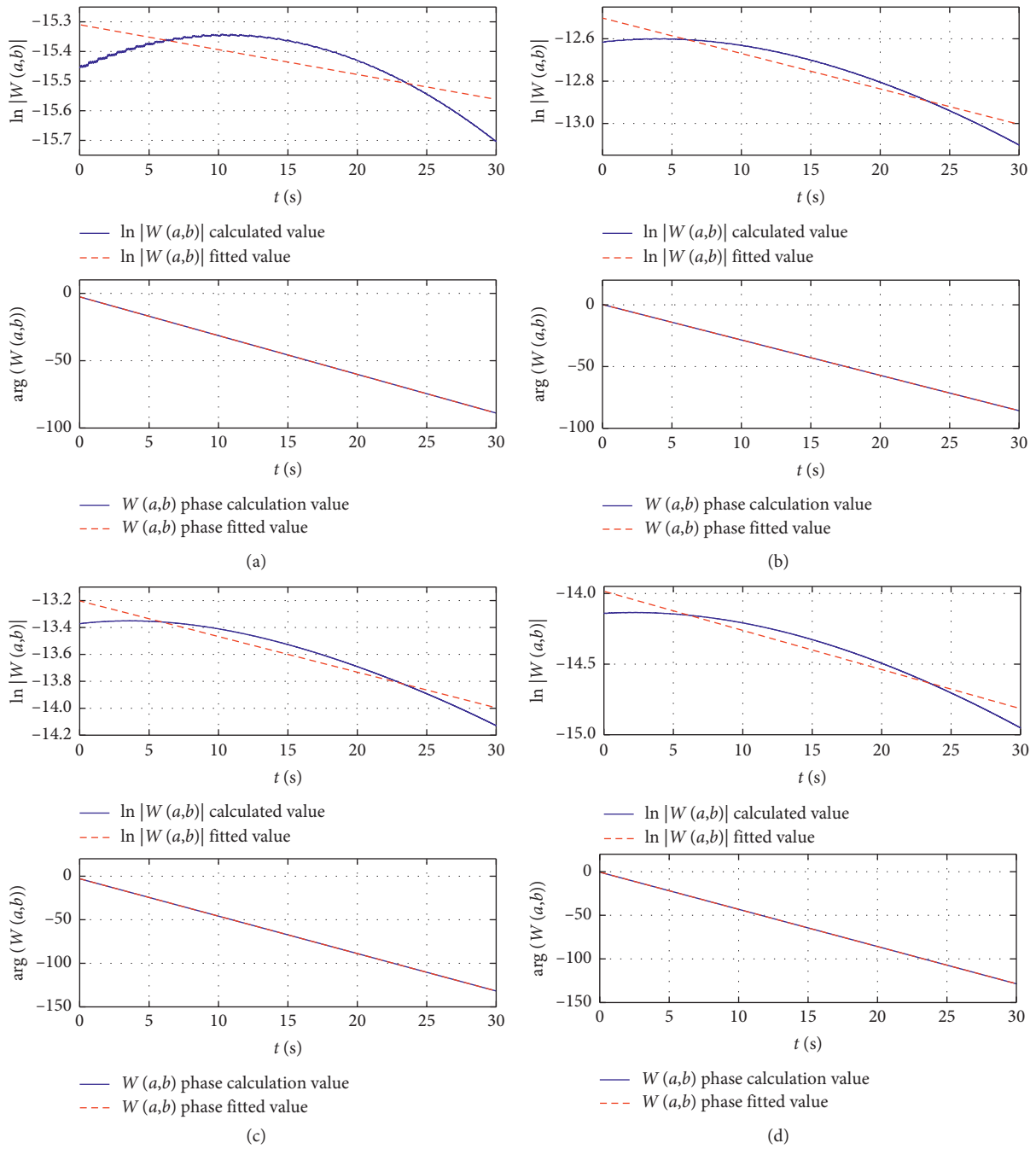


FIGURE 15: Continued.

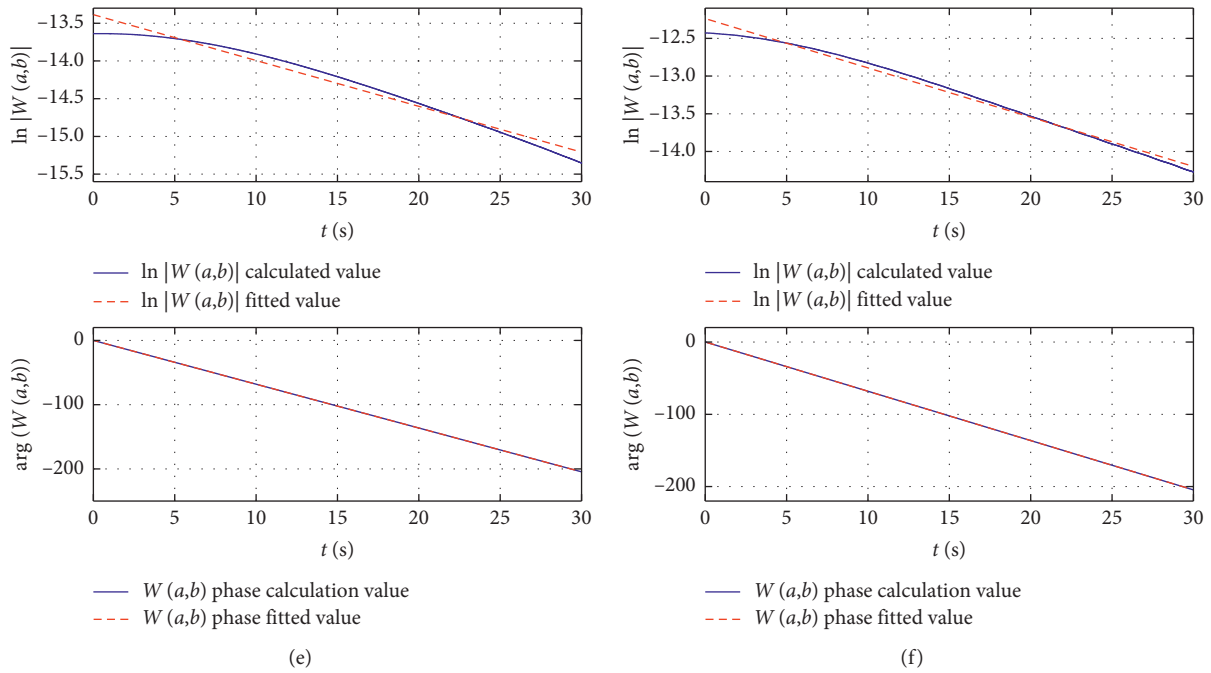


FIGURE 15: The amplitude logarithm and phase curves of the wavelet coefficients of measuring point no. 2 and no. 4 up to the third orders. (a). Measuring point 2, first order. (b). Measuring point 4, first order. (c). Measuring point 2, second order. (d). Measuring point 4, second order. (e). Measuring point 2, third order. (f). Measuring point 4, third order.

TABLE 6: Continuous wavelet transform algorithm Oujiang Bridge modal parameter identification result.

Order	Finite element results		Results of CWT algorithm		Frequency error (%)
		Frequency (Hz)	Frequency (Hz)	Damping ratio (%)	
Vertical bend	1	0.447	0.457	1.11	2.29
	2	0.677	0.682	1.13	0.73
	3	1.077	1.086	1.29	0.83
Lateral bend	1	0.318	0.321	0.90	0.86
	2	0.524	0.531	1.19	1.34
	3	0.617	0.628	1.16	1.66
	4	1.067	1.075	0.87	0.77
Torsion	1	2.455	2.513	0.13	2.34
	2	4.742	5.008	0.11	5.61

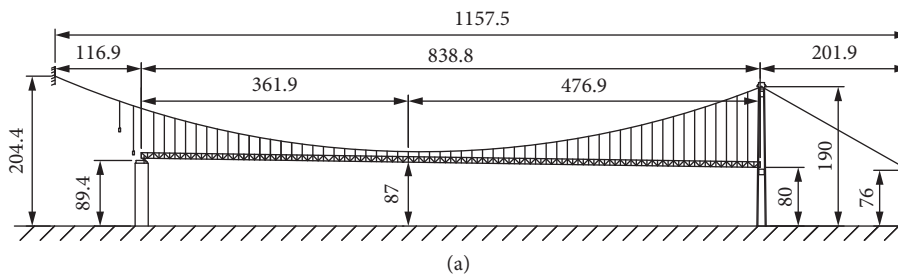


FIGURE 16: Continued.



(b)

FIGURE 16: The elevation view and model of the Jinsajiang Bridge. (a) Elevation view. (b) Bridge model placed in the wind tunnel.



FIGURE 17: The noncontact laser displacement sensor.

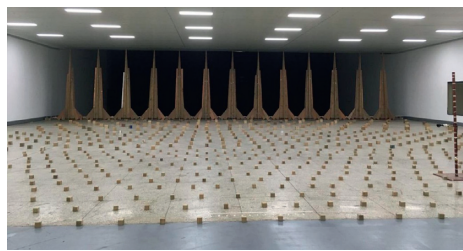


FIGURE 18: Rough element placed in wind tunnel test to simulate fluctuating wind.

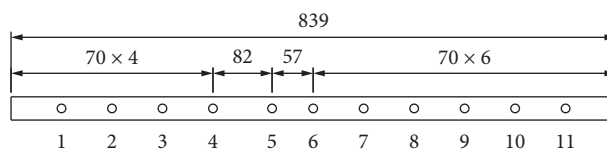
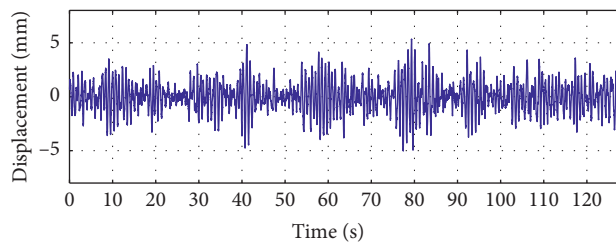
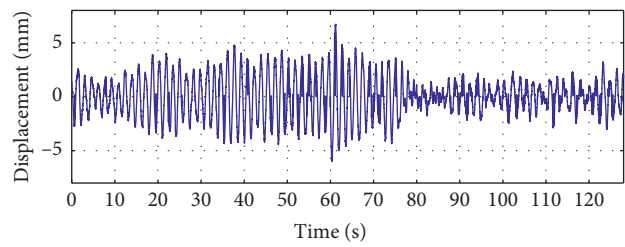


FIGURE 19: Layout of measuring points (unit: cm).



(a)



(b)

FIGURE 20: Continued.

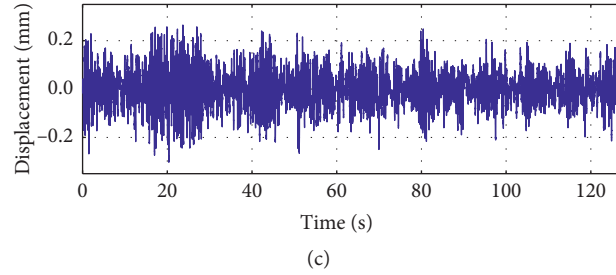


FIGURE 20: Response time history curve at point no. 6. (a) Vertical displacement. (b) Lateral displacement. (c) Torsion displacement.

TABLE 7: Model parameter identification results of Jinshajiang Bridge by CWT.

Order	Test frequency (Hz)	Results of CWT			Mode of vibration
		Frequency (Hz)	Damping ratio (%)	Error (%)	
1	1.334	1.304	1.79	2.25	Antisymmetrical vertical bend -1
2	1.838	1.780	2.01	3.16	Symmetrical vertical bend -1
3	2.452	2.407	1.45	1.84	Symmetrical vertical bend -2
4	3.023	2.893	0.64	4.30	Antisymmetrical vertical bend -2
5	0.743	0.639	0.94	14.00	Symmetrical lateral bend -1
6	3.280	3.256	1.01	0.73	Symmetrical torsion -1

5. Conclusion

In this article, an improved continuous wavelet transform method for bridge modal parameter identification under environmental excitation was proposed. The main conclusions are as follows:

- (1) With the optimal wavelet base design based on minimum Shannon entropy, it is easy to find a suitable bandwidth parameter and construct the wavelet base for the wavelet transform. This method can effectively decouple the signal intensive mode with relatively high accuracy.
- (2) The support vector machine (SVM) regression prediction method can be used to extend the measured data. Based on this, not only the characteristics of the original signal will be preserved but also the continuity and conductivity can be guaranteed. The endpoint effect of extended samples is suppressed well for all modal orders. For the first-order modal, the suppress effect of the endpoint effect is increased by 41.5%. Even for those in the higher order modal, the endpoint effect is basically eliminated after the extension.
- (3) The improved crazy clipper algorithm can extract the exact location of wavelet ridge from the approximate distribution range of wavelet ridge, whereas the traditional crazy climber algorithm can only get the approximate distribution range of wavelet ridge. Therefore, the improved crazy clipper algorithm has excellent antinoise ability and good practicability.
- (4) Taking the Oujiang Bridge and Jinshajiang Bridge as the engineering background, the improved continuous wavelet transform was applied to the identification of bridge modal parameters under

environmental excitation, and the modal parameters such as modal frequency, damping ratio, and vibration mode of the model were obtained. Compared with the theoretical values, the reliability of the improved method in the modal parameter identification of long-span bridge has been verified.

Data Availability

The data used to support the findings of this study are available from the corresponding author upon request.

Conflicts of Interest

The authors declare that they have no conflicts of interest.

Acknowledgments

This work was financially supported by the National Key Research and Development Program of China (no. 2018YFC1507800), the National Natural Science Foundation of China (nos. 51525804 and 51708464), the Fundamental Research Funds for the Central Universities (no. 2682019CX02), and the Primary Research & Development Plan of Sichuan Province (no. 2019YFG0001).

References

- [1] C. Rainieri and G. Fabbrocino, *Operational Modal Analysis of Civil Engineering Structures: An Introduction and Guide for Applications*, Springer-Verlag, New York, NY, USA, 2014.
- [2] M. Zhang, J. Yu, J. Zhang, L. Wu, and Y. Li, "Study on the wind-field characteristics over a bridge site due to the shielding effects of mountains in a deep gorge via numerical simulation," *Advances in Structural Engineering*, vol. 22, no. 14, pp. 3055–3065, 2019.

- [3] J. Zhang, M. Zhang, Y. Li, and C. Fang, "Comparison of wind characteristics at different heights of deep-cut canyon based on field measurement," *Advances in Structural Engineering*, vol. 23, no. 2, pp. 219–233, 2020.
- [4] P. Hu, Y. Han, G. Xu, C. S. Cai, and W. Cheng, "Effects of inhomogeneous wind fields on the aerostatic stability of a long-span cable-stayed bridge located in a mountain-gorge terrain," *Journal of Aerospace Engineering*, 2020.
- [5] Z. Ti, M. Zhang, Y. Li, and K. Wei, "Numerical study on the stochastic response of a long-span sea-crossing bridge subjected to extreme nonlinear wave loads," *Engineering Structures*, vol. 196, Article ID 109287, 2019.
- [6] Z. Ti, K. Wei, Y. Li, and B. Xu, "Effect of wave spectral variability on stochastic response of a long-span bridge subjected to random waves during tropical cyclones," *Journal of Bridge Engineering*, vol. 25, no. 1, Article ID 04019131, 2020.
- [7] K. Wei, J. Zhang, and S. Qin, "Experimental and numerical assessment into frequency domain dynamic response of deep water rigid-frame bridge," *Journal of Earthquake Engineering*, pp. 1–24, 2019.
- [8] J.-X. Mao, H. Wang, D.-M. Feng, T.-Y. Tao, and W.-Z. Zheng, "Investigation of dynamic properties of long-span cable-stayed bridges based on one-year monitoring data under normal operating condition," *Structural Control and Health Monitoring*, vol. 25, no. 5, Article ID e2146, 2018.
- [9] J.-X. Mao, H. Wang, Y.-G. Fu, and B. F. Spencer, "Automated modal identification using principal component and cluster analysis: application to a long-span cable-stayed bridge," *Structural Control and Health Monitoring*, vol. 26, no. 10, Article ID e2430, 2019.
- [10] N. E. Huang, Z. Shen, and S. R. Long, "A new view OF nonlinear water waves: the hilbert spectrum," *Annual Review of Fluid Mechanics*, vol. 31, no. 1, pp. 417–457, 1999.
- [11] Z. Wu and N. E. Huang, "A study of the characteristics of white noise using the empirical mode decomposition method," *Proceedings of the Royal Society of London. Series A: Mathematical, Physical and Engineering Sciences*, vol. 460, no. 2046, pp. 1597–1611, 2004.
- [12] P. Flandrin, P. Gonçalves, and G. Rilling, "Emd equivalent filter banks, from interpretation to applications," in *Hilbert-huang Transform and its Applications*, pp. 57–74, World Scientific, Singapore, 2005.
- [13] P. Flandrin, G. Rilling, and P. Goncalves, "Empirical mode decomposition as a filter bank," *IEEE Signal Processing Letters*, vol. 11, no. 2, pp. 112–114, 2004.
- [14] R. J. Gledhill, "Methods for investigating conformational change in biomolecular simulations," 2003, <https://ethos.bl.uk/OrderDetails.do?sessionid=A3B58D0D3465E8284A3969CA6CACE890?uin=uk.bl.ethos.402546>.
- [15] J.-R. Yeh, J.-S. Shieh, and N. E. Huang, "Complementary ensemble empirical mode decomposition: a novel noise enhanced data analysis method," *Advances in Adaptive Data Analysis*, vol. 2, no. 2, pp. 135–156, 2010.
- [16] G. H. Golub and C. F. V. Loan, *Matrix Computations*, JHU Press, Baltimore, MD, USA, 1996.
- [17] B. A. Pridham and J. C. Wilson, "Identification of base-excited structures using output-only parameter estimation," *Earthquake Engineering & Structural Dynamics*, vol. 33, no. 1, pp. 133–155, 2004.
- [18] G. A. Smith and A. J. Robinson, *A Comparison between the EM and Subspace Identification Algorithms for Time-Invariant Linear Dynamical Systems*, University of Cambridge, Cambridge, UK, 2000.
- [19] P. van Overschee and B. L. de Moor, *Subspace Identification for Linear Systems: Theory—Implementation—Applications*, Springer Science & Business Media, New York, NY, USA, 1996.
- [20] J.-H. Weng, *Application of Subspace Identification in System Identification and Structural Damage Detection*, 2010.
- [21] J.-H. Weng, C.-H. Loh, J. P. Lynch, K.-C. Lu, P.-Y. Lin, and Y. Wang, "Output-only modal identification of a cable-stayed bridge using wireless monitoring systems," *Engineering Structures*, vol. 30, no. 7, pp. 1820–1830, 2008.
- [22] A. Grossmann and J. Morlet, "Decomposition of hardy functions into square integrable wavelets of constant shape," *SIAM Journal on Mathematical Analysis*, vol. 15, no. 4, pp. 723–736, 1984.
- [23] K. Gurley and A. Kareem, "Applications of wavelet transforms in earthquake, wind and ocean engineering," *Engineering Structures*, vol. 21, pp. 149–167, 1999.
- [24] T. Kijewski and A. Kareem, "Wavelet transforms for system identification in civil engineering," *Computer-Aided Civil and Infrastructure Engineering*, vol. 18, no. 5, pp. 339–355, 2003.
- [25] J. Lardies and S. Gouttebroze, "Identification of modal parameters using the wavelet transform," *International Journal of Mechanical Sciences*, vol. 44, no. 11, pp. 2263–2283, 2002.
- [26] H. Sarparast, M. R. Ashory, M. Hajiazizi, M. Afzali, and M. M. Khatibi, "Estimation of modal parameters for structurally damped systems using wavelet transform," *European Journal of Mechanics—A/Solids*, vol. 47, pp. 82–91, 2014.
- [27] T.-H. Yi, H.-N. Li, and G. Wang, "Structural modal parameter identification based on wavelet transform," *Journal of Vibration Engineering*, vol. 19, no. 1, pp. 51–56, 2006.
- [28] H. Wang, J. X. Mao, J. H. Huang, and A. Q. Li, "Modal identification of sutong cable-stayed bridge during typhoon Haikui using wavelet transform method," *Journal of Performance of Constructed Facilities*, vol. 30, no. 5, Article ID 04016001, 2016.
- [29] B. Yan and A. Miyamoto, "A comparative study of modal parameter identification based on wavelet and Hilbert-Huang transform," *Computer-Aided Civil and Infrastructure*, vol. 21, no. 1, pp. 9–23, 2005.